Journal of
Materials Chemistry A

ROYAL SOCIETY
OF CHEMISTRY

PAPER

View Article Online
View Journal | View Issue

Check for updates

Cite this: *J. Mater. Chem. A*, 2025, **13**, 40874

# Organic semiconductor frameworks integrating bay-substituted perylene bisimides as screw dislocation units in onion-like π–π stacked architectures†

Leonardo Cognigni,[a] Jintao Liu,[a] Stefano Magliocco,[b] Gloria Berlier,[b] Silvia Bordiga,[b] Silvia Bracco,[c] Angiolina Comotti,[c] Francesco Rigodanza,[a] Thomas Gobbato,*[ad] Daniele Rosa-Gastaldo*[a] and Marcella Bonchio*[ade]

Imine-linked covalent organic frameworks (COFs) are built with precision chemistry control, where the tetra-*p*-CHO-aryloxy bay-substituted **PBI-1** serves as a rylene chromophore subunit encoding (i) a broad visible light cross-section ($\varepsilon_{\lambda 552\ \mathrm{nm}} = 42\,000\ \mathrm{L\ mol^{-1}\ cm^{-1}}$); (ii) an excited state redox manifold ($E(\mathbf{PBI\text{-}1}^{*/\cdot-}) = 1.82$ V *vs.* NHE, $E(\mathbf{PBI\text{-}1}^{\cdot+/*}) = -0.43$ V *vs.* NHE); (iii) a dynamic chiral distortion of the aromatic core with a dihedral angle of up to 33°; and (iv) two tertiary amines as *N*-imide terminals favoring proton-coupled charge transfer mechanisms in aqueous media. **PBI-1-COFs** are designed herein following an isoreticular expansion strategy based on the elongation of polyaryldiamine linkers ($n = 1$–3 as Ph, *b*Ph, and *t*Ph), where convergent FT-IR, ssNMR, PXRD, TEM and SEM evidence points to a slip-stacked arrangement of the 2D-COF layers, likely induced by the conformational distortion of the **PBI-1** cores, resulting in a prevalent J-type coupling scheme and a distinct red-shift of the material absorption (up to 700 nm), optical bandgaps of ∼1.9 eV, and a morphological progression from onion-like, curved π–π stacked domains to fully folded spheroidal structures (quasi-monodispersed particles with $D = 700 \pm 100$ nm). *In situ* polymerization of high surface area 3D-tungsten oxide nanosheets ($WO_3$ 3D-NS) affords robust photoanodes integrating the n-type COF semiconductor layer capable of record photocurrent outputs (up to $590 \pm 50\ \mu\mathrm{A\ cm^{-2}}$) under green-light irradiation (1 sun, $\lambda > 490$ nm), probed with anionic hydroquinone shunts (an applied bias of 0.8 V *vs.* RHE) and favored by a preferential host–guest response due to complementary charge interactions mapped by NMR-DOSY and FT-IR spectroscopy.

Received 29th June 2025
Accepted 5th August 2025

DOI: 10.1039/d5ta05253j

rsc.li/materials-a

## 1. Introduction

Organic semiconductors (OSCs) are emerging as a ground-breaking class of molecular materials at the frontier of opto-electronics and photocatalysis research due to their unique exploration of chemical space in terms of composition, structural hierarchy and morphology at multi-scale levels.[1] The OSC function is also regulated across dimensional scales, ranging from the stereo-electronics of molecular sub-units and their multi-site interactions within the material network, to defects or structural dislocations generated at the micro- and meso-scopic scales and transferred to the short- or long-range arrangement of the OSC at the macro-scopic scale.[2] Notably, the broad inventory of molecular synthons and bond connectivities offers a rich portfolio for precision chemistry methods to regulate the overall life-cycle sustainability of OSCs, including the initial synthetic steps, scale-up fabrication, low-cost solution processability, and the end phase of de-construction and recycling of exhausted materials. Considering the molecular bottom-up advantage to drive materials innovation, OSC optimization is appealing for renewable energy applications such as photocatalytic water splitting and/or redox flow batteries.[3–7]

In the field of photoconductive OSCs, one key challenge is related to their light-harvesting cross-section, requiring the engineering of extended molecular architectures based on highly conjugated aromatic cores and their assembly into π-stacked periodic domains.[3,8] In particular, solar energy

---

[a] Department of Chemical Sciences, University of Padova, Via Marzolo 1, 35131 Padova, Italy. E-mail: thomas.gobbato@unipd.it; daniele.rosagastaldo@unipd.it; marcella.bonchio@unipd.it

[b] Department of Chemistry, NIS and INSTM Centres, University of Turin, via Giuria 7, 10135 Turin, Italy

[c] Department of Materials Science, University of Milano-Bicocca, Via R. Cozzi 55, 20125 Milano, Italy

[d] Interuniversity Consortium on Materials Science and Technology, INSTM UdR Padova, Via Marzolo 1, 35131 Padova, Italy

[e] Institute of Membrane Technology ITM-CNR, Via Marzolo 1, 35131 Padova, Italy

† Dedicated to Prof. Petra Rudolf outstanding career achievements.

conversion and storage call for tailored OSC π–π networks that integrate aromatic chromophores with high extinction coefficients in the visible range ($\varepsilon_{\lambda>500\ \mathrm{nm}} = 10^5$), heteroatom-based nodes (N, O, S, *etc.*) and shape-induced anisotropy.[9–15] All these factors are known to play a decisive role in tuning the electron distribution, the orientation of molecular dipoles and their coupling system, with a major impact on the OSC energy levels (band-gap) and the photodynamics of charge carrier generation and transport.[4,9,10] In view of these challenges, the class of perylene bisimide (PBI) chromophores stands out due to their strong visible-light absorption ($\varepsilon_{\lambda500\ \mathrm{nm}} > 30\,000$), large transition dipole moment, multi-electron redox manifold, and π-stacked supramolecular interactions, together with aggregate-dependent photodynamics and superior photostability among organic pigments.[16–18] PBI functionalization can be performed at the nitrogen site of the imide node and at the two sites of the perylene core, namely, at the "*bay*" (1, 6, 7, 12) and "*ortho*" (2, 5, 8, 11) positions (Fig. 1A), thus enabling precise control over the molecular stereo-electronics dictating geometries, optical properties, supramolecular interactions and aggregate morphologies.[19] Notably, upon the full substitution of the bay area, the steric hindrance of the perylene core leads to core-twisted atropisomers (P- and M-enantiomers) that can interconvert in solutions depending on the dihedral angle constraint and racemization kinetics.[20–23] Building on these concepts, OSCs that encode the PBI prerogative can be designed as covalent organic frameworks (PBI-COFs) through the dynamic formation of covalent bonds with precise control over the composition, periodicity, and layered π–π stacking of the PBI building blocks. Despite the clear potential of PBI-COFs as photoresponsive platforms, the functionalization constraints of the perylene core and the low solubility of π–π supramolecular aggregates pose severe synthetic challenges. Seminal attempts have recently focused on imide- or *ortho*-substituted PBIs exhibiting a planar core and a π–π stacked 2D architecture.[24–27]

Herein, we present an unprecedented series of imine-linked COFs incorporating a novel bay-substituted PBI (**PBI-1**), specifically designed for enhanced visible light absorption ($\varepsilon_{\lambda552\ \mathrm{nm}} = 42\,000\ \mathrm{L\ mol^{-1}\ cm^{-1}}$) and a tailored excited state oxidation potential ($E(\mathbf{PBI\text{-}1}^{*/\cdot-}) = 1.82$ V *vs.* NHE), featuring a symmetric substitution scheme with two tertiary amines and four *p*-CHO aryl ether substituents, respectively, at the imide and bay positions (Fig. 1A). Noteworthy, the **PBI-1** core is expected to display a propeller-type distortion of the aromatic core, with a dihedral angle of up to 33°, which implies the occurrence of atropisomer interconversion and of their π–π organization upon COF formation.[20] Our results include the use of aryl-1,4-diamine linkers with increasing length of the linear aryl-spacer. The resulting **PBI-1-COFs** integrate N-rich imine and tertiary amine sites that undergo protonation in acidic media, thus evolving to positively charged ionic COF domains with a recognition ability towards anionic additives/co-factors and facilitating proton transfer and water access. It turns out that **PBI-1-COFs** are endowed with (i) screw dislocations evolving to onion-like π-stacked crystalline arrangements; (ii) a visible-light cross-section extending up to 700 nm; (iii) an optical band gap of $E_g = 1.9 \pm 0.1$ eV, potentially suitable for overall water splitting; and (iv) favorable interactions with anionic hydroquinones used

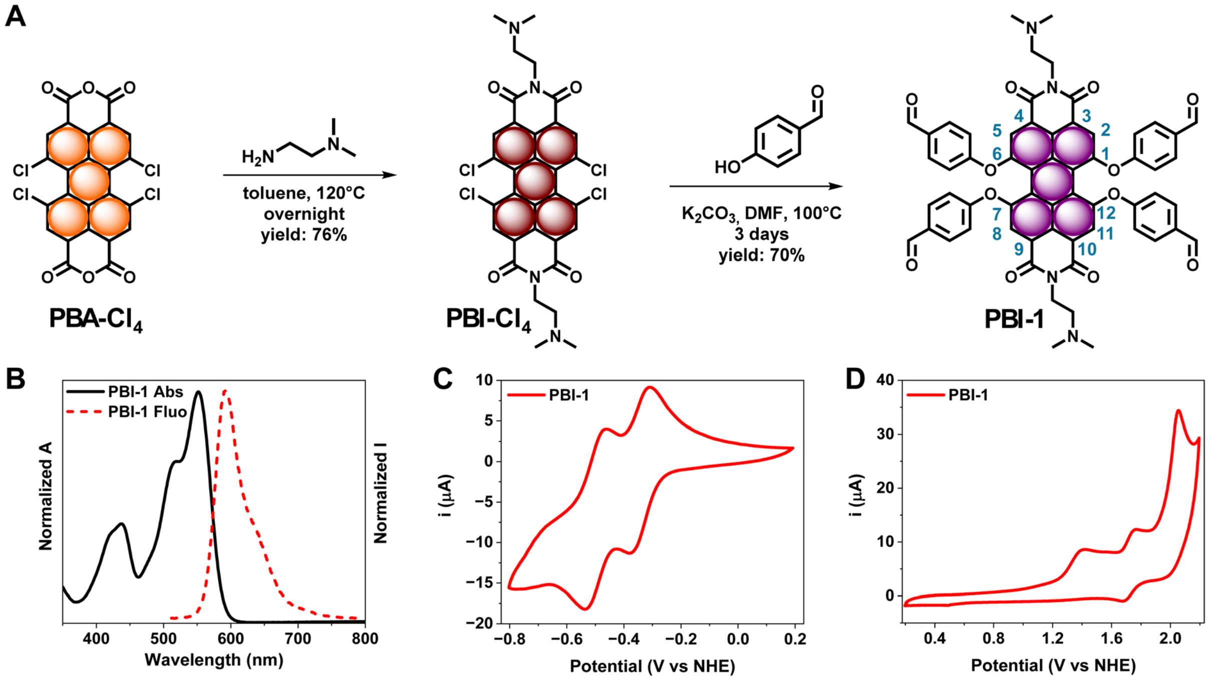

Fig. 1 (A) Synthetic pathway for PBI-1 with detailed reaction conditions. Numbering of the perylene core positions is reported for PBI-1. (B) Normalised UV-vis absorption (black trace) and emission (red dashed trace, excitation wavelength = 530 nm) spectra of PBI-1 (25 µM in DCM). Cyclic voltammograms of PBI-1 (1 mM in DCM, 0.1 M $\mathrm{TBAPF_6}$, scan rate = 100 mV $\mathrm{s^{-1}}$, glassy carbon working electrode, Ag/AgCl reference electrode, and Pt counter electrode) scanning from (C) −0.8 to 0.2 V *vs.* NHE and (D) 0.2 to 2.2 V *vs.* NHE.

as photo-redox shunts, as probed *via* nuclear magnetic resonance diffusion ordered spectroscopy (NMR-DOSY) and FT-IR spectroscopy.

The **PBI-1-COF** series are engineered on three-dimensional tungsten oxide nanosheets ($WO_3$ 3D-NS) by direct *in situ* growth.[28] The $WO_3$ substrate offers conduction and valence band edges compatible with the photoredox potentials of PBI-based OSCs.[29–31] To the best of our knowledge, this is the first example of **PBI-COF@WO$_3$** heterojunctions fabricated as photoanodes and operating in water (1 M $H_2SO_4$) with photocurrent densities up to 590 ± 50 μA cm$^{-2}$, minimal transient recombination and only 3% loss for >10 on-off light cycles. During long-term photoelectrolysis (>20 h), the photocurrent loss amounts to only 16% under continuous illumination ($\lambda$ > 490 nm), showing the remarkable stability of the **PBI-COF@WO$_3$** photoanode.

The molecular regulation of hydrophilicity and ionic properties, together with the favorable overlap with the solar spectrum, of these novel **PBI-1-COFs** indicates the definite potential of bay-substituted PBIs to modulate crystalline frameworks as advanced OSCs.

## 2. Results and discussion

### 2.1 PBI-1-COFs synthesis and characterization

Tetra-aldehyde 1,6,7,12-tetra(4-formyl-phenoxy)-3,4,9,10-perylenetetracarboxylic bisimide (**PBI-1**) was synthesized by a two-step protocol by reacting the tetra-chlorinated perylene bisanhydride (**PBA-Cl$_4$**) with *N*,*N*-dimethylethylenediamine to yield the parent bisimide precursor (**PBI-Cl$_4$**),[32] followed by nucleophilic aromatic substitution with *p*-hydroxybenzaldehyde, leading to the **PBI-1** synthetic target (Fig. 1A). Characterization by FTIR, high-resolution mass spectrometry, and NMR spectroscopy confirms the expected substitution pattern of the perylene core with four *p*-benzaldehyde terminals (SI, Sections S2 and S3). In agreement with literature results, fast interconverting atropisomers are expected due to the twisted perylene core.

The UV-vis spectrum of **PBI-1** in dichloromethane (DCM) shows an absorption onset at $\lambda_{\text{onset}} = 590$ nm, with the main absorption band maximum at 552 nm ($A_{0-0}$, $\varepsilon_{\lambda 552} = 42\,000$ L mol$^{-1}$ cm$^{-1}$) ascribed to the $S_0$–$S_1$ transition and a vibronic progression ($A_{0-1}$, $\varepsilon_{\lambda 519} = 29\,000$ L mol$^{-1}$ cm$^{-1}$) at 519 nm. The broader absorption band between 400 and 500 nm results from the $S_0$–$S_2$ transition (Fig. 1B).[33] The $A_{0-1}/A_{0-0}$ ratio of 0.69 is typical of a monomeric state.[34] The resulting emission spectrum exhibits a mirror-image profile relative to the $S_0$–$S_1$ absorption band, with a maximum at 592 nm and a fluorescence quantum yield $\Phi_{\text{FL}}$ of 0.94. Relative to the unsubstituted PBI reference, a bathochromic shift of ~30 nm is observed in both absorption and fluorescence spectra, which is consistent with the electron-donating properties of the four aryloxy substituents.[35,36]

The cyclic voltammetry (CV) of **PBI-1** in DCM (Fig. 1C) shows two reversible reduction waves at $E_{1/2} = -0.32$ V and $E_{1/2} = -0.49$ V *vs.* NHE, resulting in the formation of the PBI radical mono- and di-anion. The anodic sweep (Fig. 1D) shows three oxidations: the first one at 1.40 V *vs.* NHE is associated with the irreversible oxidation of the dimethylamine residue, while the two reversible peaks at $E_{1/2} = 1.72$ V and $E_{1/2} = 2.00$ V *vs.* NHE are ascribed to the stepwise oxidation of the perylene core and substituents, respectively.[17,37–39] According to these data, upon visible light absorption, **PBI-1** can generate excited states with related redox potentials of E(**PBI-1**$^{*/\cdot-}$) = 1.82 V *vs.* NHE and E(**PBI-1**$^{\cdot+/*}$) = −0.43 V *vs.* NHE (SI, Section S1), thus providing a key molecular building block for photocatalytic frameworks.[40] To this aim, a representative library of imine-based covalent organic frameworks (**PBI-1-COFs**) was obtained by reacting **PBI-1** with linear aryldiamine linkers of increasing length, namely, 1,4-phenylenediamine (**Ph**), 4,4′-biphenyldiamine (***b*Ph**), and 4,4″-diamino-*p*-terphenyl (***t*Ph**), under solvothermal conditions in a 1,2-dichlorobenzene/*tert*-butanol mixture (1,2-DCB : *t*-BuOH = 50 : 50) with acetic acid (6 M AcOH) at 120 °C for 3 days. This synthetic protocol proved to be effective across the diverse aryldiamine linkers, yielding, respectively, **PBI-1-COF-Ph**, **PBI-1-COF-*b*Ph**, **PBI-1-COF-*t*Ph** (Fig. 2A, SI, Section S2.6).[41]

The characterization of the first homologue in the series ($n$ = 1, **PBI-1-COF-Ph**, Fig. 2A) is discussed herein to showcase the key features of this class of organic frameworks. FT-IR evidence supports the formation of the imine-based structure by the appearance of a new band at 1623 cm$^{-1}$, characteristic of the C=N bond stretching.[42–44] At the same time, the **PBI-1** carbonyl absorption, observed at approximately 1700 cm$^{-1}$ (overlapping peaks of aldehyde and imide C=O asymmetric stretching), is significantly reduced, as expected, due to aldehyde conversion during the solvothermal process.[45] Furthermore, the absence of the aldehyde C–H stretching band at *ca.* 2800 cm$^{-1}$ supports the complete imine condensation and the formation of the imine-linked framework (SI, Section S4.1, Fig. S1). Similar conclusions are drawn for the **PBI-1-COF-*b*Ph** and **PBI-1-COF-*t*Ph** analogues (SI, Section S4.1, Fig. S2 and S3).

Solid-state NMR spectroscopy (ssNMR) confirms the formation of the covalent framework, based on the $^{13}$C magic angle spinning (MAS) NMR spectra collected for the unlabeled series of **PBI-1-COF** derivatives and performed with a recycle delay of 60 s. The observed multiplicity of signals is in complete agreement with the expected pattern of **PBI-1** and the corresponding aryldiamino components (Fig. 2B). In the 120–140 ppm region, the two signals at 138 ppm (blue area) and 127 ppm (red area) are assigned to the *p*-phenylene units, which increase from **PBI-1-COF-*b*Ph** to **PBI-1-COF-*t*Ph** (Fig. 2B, Section S4.2, Fig. S4) due to the presence of the biphenyl and terphenyl polymerization linkers, respectively.[46] The formation of the imine-based connectivity is unveiled by comparing the $^{13}$C CP-MAS spectra collected at contact times of 2 ms and 50 μs (Fig. 2B, inset). At a 2 ms contact time, the signal lineshape in the range of 145–165 ppm results from the partial superimposition of four resonances, arising from deshielded environments and including the imide (C=O), aryl-oxy ($C_{\text{Ar}}$–O), imine (C=N) and aryl-amino ($C_{\text{Ar}}$–N) positions. Noteworthy, at a shorter contact time (50 μs), only one signal stands out at about 157.2 ppm, which univocally identifies the presence of a carbon directly bonded to a hydrogen atom and whose chemical shift indicates the formation of the imine linkage (color code in Fig. 2C).[46] The comparison of the intensity of the signals at about 190 ppm

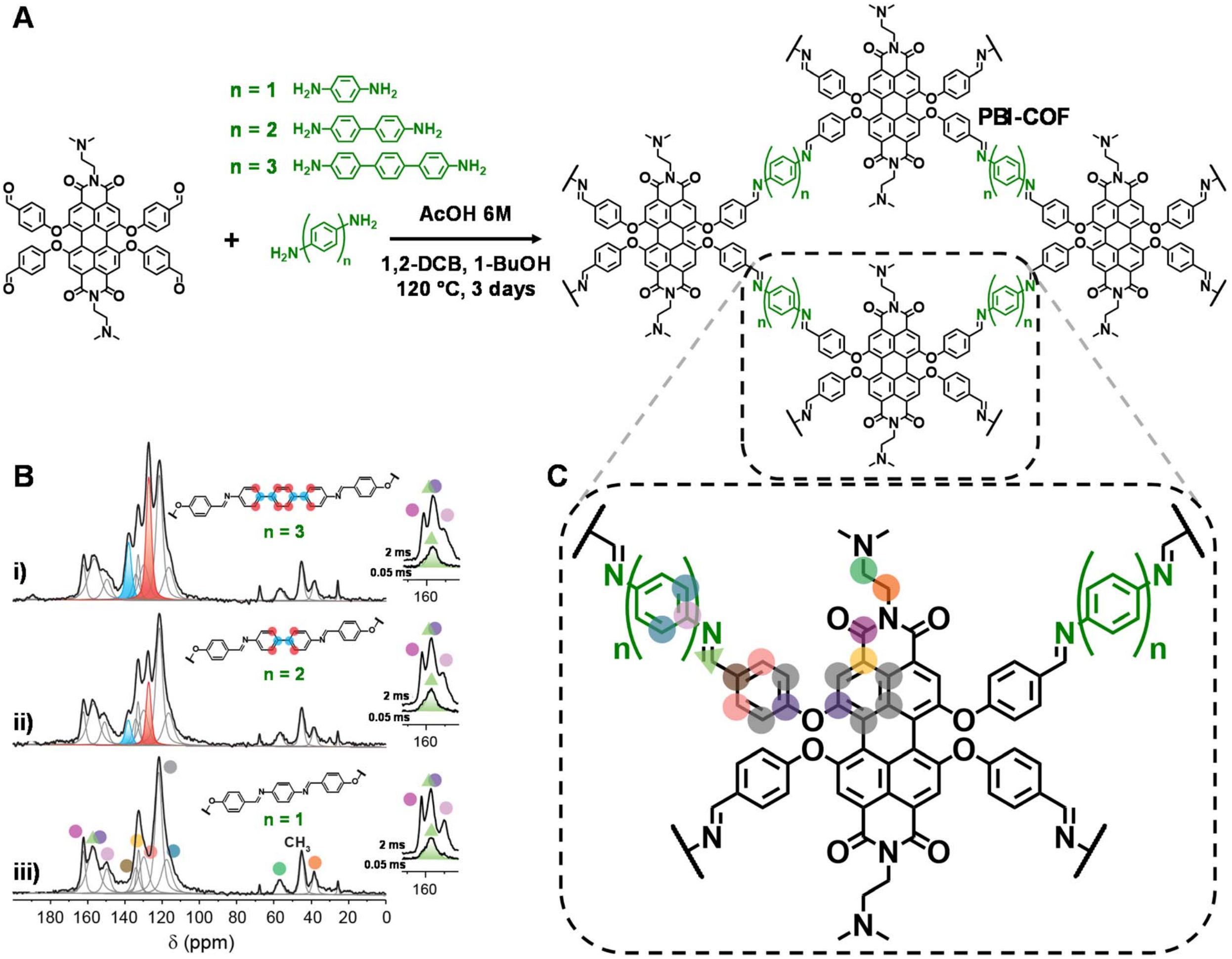

Fig. 2 (A) Representative molecular structures and synthetic pathway for **PBI-1-COF** materials. **PBI-1** was reacted with the corresponding diamine in a 50 : 50 mixture of 1,2-dichlorobenzene : 1-butanol with a catalytic amount of 6 M acetic acid for 3 days at 120 °C in closed glass tube (SI, Section S2 for detailed conditions). (B) Quantitative $^{13}$C SPE MAS spectra collected at 12.5 kHz with a recycle delay of 60 s for **PBI-1-COF-*t*Ph** ($n = 3$, panel i), **PBI-1-COF-*b*Ph** ($n = 2$, panel ii), and **PBI-1-COF-Ph** ($n = 1$, panel iii). Inset: highlighted 160 ppm regions of $^{13}$C CP MAS NMR spectra collected with 0.05- and 2 ms contact times. (C) Molecular structure of the **PBI-1-COF** repetitive unit with colour codes for signal assignment.

(unreacted aldehyde residues) with the one of the imine network allows us to estimate polymerization yields as high as 92% for **PBI-1-COF-Ph**, 89% for **PBI-1-COF-*b*Ph** and 90% for **PBI-1-COF-*t*Ph** (SI, Section S4.2, Tables S1–S3). Indeed, the relative integration of signals pertaining to the **PBI-1** core *versus* the *p*-phenylene linker results in the expected 1 : 2 polymerization ratio (SI, Tables S1–S3, SI). An analogous stoichiometry ratio is obtained by solution $^1$H-NMR analysis performed on COF samples digested in a 3 : 1 mixture of TFA-*d* and $D_2O$, adapting an approach used for metal–organic frameworks (MOFs, SI, Section S4.3, Fig. S5, Table S4).[47]

Powder X-ray diffraction (PXRD) analysis yields similar reflection patterns for the **PBI-1-COF** series, showing a peak shift to lower $2\theta$ angles upon increasing the length of the aryldiamino spacer ($n = 1$–3, Fig. 3A and SI, Section S4.4, Fig. S6–S8). In particular, diffraction peaks are observed in two distinct series at $2\theta = 4.13°$, 3.41°, 2.92° and 7.96°, 6.58° and 5.74°, followed by broad features at $2\theta = 11.14°$, 9.66°, 8.50° and 21.4°, 20.7°, 19.6°, respectively, for **Ph**, ***b*Ph**, and ***t*Ph** COF linkers (Fig. 3A). These broad features are generally ascribed to multiple factors including the COF layer slippage and the presence of diverse crystalline domains or amorphous framework regions.[48] These results are consistent with the expected isoreticular expansion of the COF structure driven by the elongation of the aryldiamino linker.[49,50] Structural models (Fig. 3B and C) have been considered based on (i) the tetra-*vs.* di-topic geometry of molecular junctions;[51] (ii) the dynamic distortion of **PBI-1**, with the dihedral angle in the range of 0–33°, and its confinement within the covalently locked framework; and (iii) an eclipsed AA stacking of the 2D-COF layers. In particular, the impact of the **PBI-1** core distortion, in combination with the stereo-electronic constraints imposed by the covalent framework, has been addressed by modelling the **PBI-1-COF-Ph** with two distinct unit cells, representing two limiting cases: $\varphi = 0°$ (planar core) and $\varphi = 33°$ (twisted core) (Fig. 3A–C).

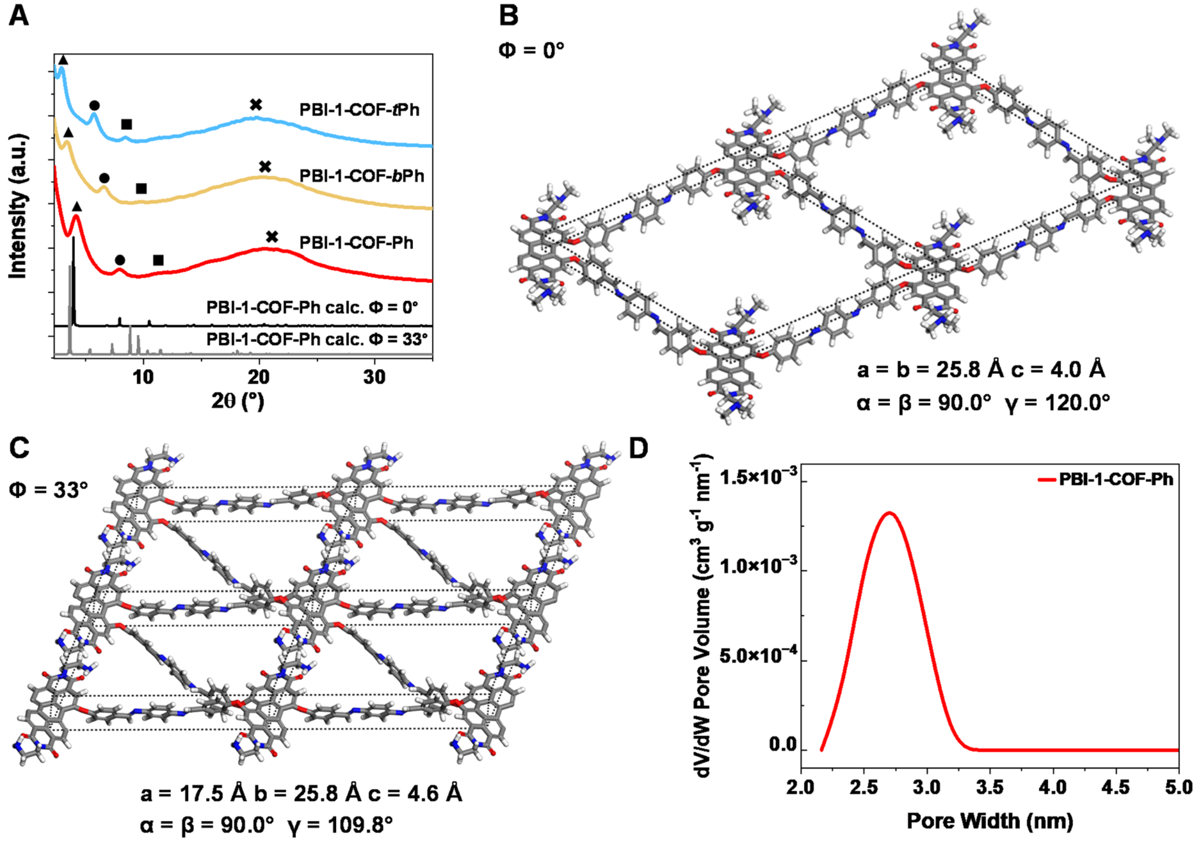

Fig. 3 (A) Experimental PXRD patterns of **PBI-1-COF-Ph** (red trace), **PBI-1-COF-*b*Ph** (yellow trace), and **PBI-1-COF-*t*Ph** (blue trace) along with the calculated PXRD patterns (black trace, $\varphi = 0°$; grey trace, $\varphi = 33°$) obtained by modelling an AA layer stacking mode for **PBI-1-COF-Ph**. (B) **PBI-1-COF-Ph** hexagonal unit cell and related parameters with $\varphi = 0°$. (C) **PBI-1-COF-Ph** triclinic unit cell and related parameters with $\varphi = 33°$. Both models were built and optimized using the Accelerys Material Studio 7.0 software package. (D) Pore size distribution of **PBI-1-COF-Ph** obtained from $N_2$ gas-volumetric measurements (DFT pore size method).

Pawley refinements against the experimental PXRD pattern of **PBI-1-COF-Ph** generate hexagonal ($\varphi = 0°$) and triclinic ($\varphi = 33°$) unit cells, in agreement with the loss of symmetry induced by the twisted core. The first diffraction peak for both crystal systems is assigned to the 100 plane, pointing to a long-range periodicity along the *ab* plane in the **PBI-1-COFs** structure.[52] The comparison of the experimental PXRD data with the simulated patterns of fully AA-stacked arrangements yields comparable refinement parameters for both models (Pawley refinement for $\varphi = 33°$, $R_{wp} = 2.78\%$, $R_p = 2.17\%$; and for $\varphi = 0°$, $R_{wp} = 2.69\%$, $R_p = 2.10\%$), suggesting the possible coexistence of planar and twisted configurations within the COF architecture. This observation is also verified for **PBI-1-COF-*b*Ph** ($\varphi = 33°$, $R_{wp} = 1.85\%$, $R_p = 1.57\%$; $\varphi = 0°$, $R_{wp} = 1.76\%$, $R_p = 1.15\%$) and **PBI-1-COF-*t*Ph** ($\varphi = 33°$, $R_{wp} = 1.16\%$, $R_p = 0.93\%$; $\varphi = 0°$, $R_{wp} = 1.58\%$, $R_p = 0.90\%$) (SI, Secion S4.4, Fig. S6–S8).[53,54] Accordingly, the pore dimensions, extracted from the structural models and PXRD fittings, follow the trend: **PBI-1-COF-Ph** ($\varphi = 0°$, $a = b = 25.8$ Å, $d_{calc} = 3.8$ nm, $\varphi = 33°$, $a = 17.5$ Å, $b = 25.8$ Å, $d_{calc} = 1.6$ nm) < **PBI-1-COF-*b*Ph** ($\varphi = 0°$, $a = b = 29.8$ Å, $d_{calc} = 4.6$ nm, $\varphi = 33°$, $a = 20.7$ Å, $b = 30.5$ Å, $d_{calc} = 1.8$ nm) < **PBI-1-COF-*t*Ph** ($\varphi = 0°$, $a = b = 34.3$ Å, $d_{calc} = 5.3$ nm, $\varphi = 33°$, $a = 24.3$ Å, $b = 35.5$ Å, $d_{calc} = 2.3$ nm).

The porosity and surface area of the **PBI-1**-based framework were examined by $N_2$ adsorption isotherms at 77 K using **PBI-1-COF-Ph** as a representative case (SI, Section S4.5, Fig. S9). **PBI-1-COF-Ph** displays a type-V $N_2$ sorption isotherm with a small hysteresis typical of weak interactions between the adsorbate and the adsorbent.[24] A pore size distribution is obtained that is centred at $d_{exp} = 2.6$ nm, typical of small-sized mesoporous COFs (2–4 nm), as predicted from the simulated structures. Moreover, Brunauer–Emmett–Teller analysis (BET) yields a surface area as low as 11 $m^2\ g^{-1}$, which can be ascribed to the slip-stacking arrangement of the framework layers,[24,25,48,54] likely due to the **PBI-1** core distortion and indicated by the occurrence of broad reflexes at $2\theta > 19°$.[48,54–56]

The COF morphology was investigated by transmission electron microscopy (TEM, Fig. 4A and B) and scanning electron microscopy (SEM, Fig. 4C and D) experiments. The TEM images of **PBI-1-COF-Ph** reveal curved parallel fringes, which are often associated with onion-like or nanotube-like architectures in 2D materials.[57,58]

These features show an interlayer spacing of 0.34 ± 0.01 nm, consistent with π–π stacking interactions between stacked COF layers (typically 0.30–0.40 nm).[59–61] Moreover, fingerprint-like regions and the corresponding electron diffraction patterns

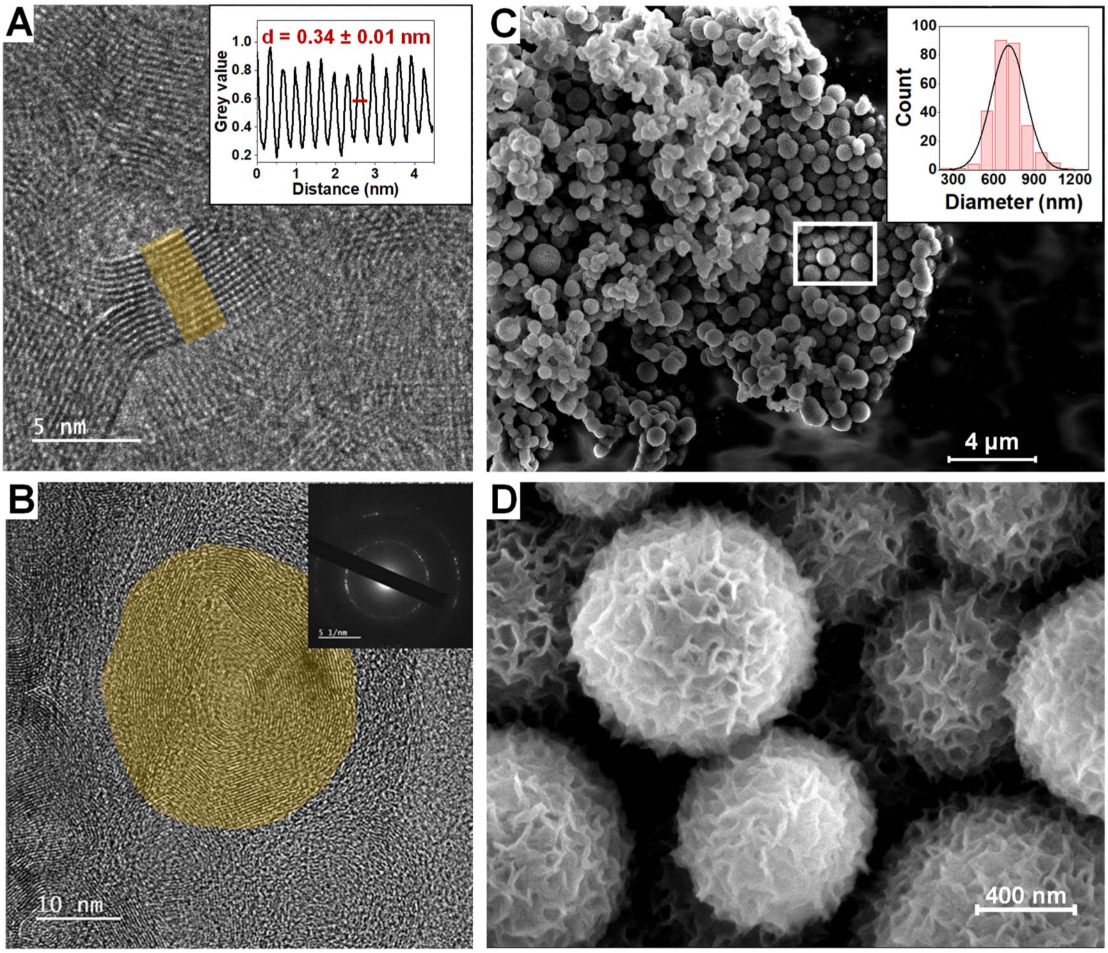

Fig. 4 (A) HR-TEM image showing the periodic curved structure of **PBI-1-COF-Ph**. Inset: plot profile of the highlighted region showing the typical distances of the $\pi-\pi$ stacking ($d = 0.34 \pm 0.01$ nm). (B) HR-TEM image of the **PBI-1-COF-Ph** domain showing extended curvature of the material. Inset: electron diffraction image. (C) Large-scale SEM image of **PBI-1-COF-Ph** showing a spherical structure. Inset: statistical analysis of the diameter of **PBI-1-COF-Ph** spheres ($d = 700 \pm 100$ nm). (D) Close-up SEM image of **PBI-1-COF-Ph** spherical particles.

confirm the presence of screw dislocations, as recently reported in the field of 2D materials, where the layer stacking mode can result from a combination of AA, AB and/or "saddle point" contacts.[56,62,63] No appreciable curved patterns are observed for **PBI-1-COF-*b*Ph** and **PBI-1-COF-*t*Ph** in TEM experiments (SI, Section S4.6, Fig. S10), likely associated to more flexible networks. The intrinsic chiral distortion of the **PBI-1** synthon can foster the nucleation of curved COF seeds, which then grow up to coalesce into extended structures in the micrometric domain. Noteworthy, **PBI-1-COF-Ph** evolves into well-dispersed spherical microparticles with an average diameter of $D = 700 \pm 100$ nm, and surface corrugation by staggered nanosheets, likely formed at an intermediate stage and gradually folding into the spheroid structure (Fig. 4D).[64–67] Isoreticular **PBI-1-COF-*b*Ph** and **PBI-1-COF-*t*Ph** exhibit a mixed morphology with both spherical and rod-like domains (SI, Section S4.7, Fig. S11), thus indicating that the COF morphology is likely dictated by an interplay of factors including the steric repulsion of the PBI substituents, combined with the linker flexibility of the COF backbone tuned by the conformational dynamics of the bay-substituted PBI core.[68,69]

With the aim of enhancing the framework's crystallinity and to verify the reproducibility of the reaction protocols, a systematic screening of the synthetic parameters was conducted for **PBI-1-COF-Ph**, including solvent variation, acid catalyst, reaction time, and heating method (solvothermal or microwave-assisted; SI, Section S4.8, Table S5). Based on comparative PXRD analysis (SI, Section S4.8, Fig. S12 and S13), no significant improvement in the COF crystallinity is achieved within the explored synthetic space.

### 2.2 Optical properties of PBI-1-COFs at organic–inorganic semiconductor-heterojunctions

The four-aryloxy electron-donating bay substituents of **PBI-1** are instrumental to enhance the electron density of the aromatic core, resulting in a redshifted UV-vis absorption with respect to imide- or ortho-functionalized PBIs (Fig. 1B).[70] The stereo-electronic impact of the **PBI-1** domains framed within the COF environment was probed as the organic semiconductor layer on tungsten-oxide ($WO_3$) photoanodes. The $WO_3$ interface is known to provide edge positions of conduction and valence bands (CB and VB, respectively), matching the photoredox manifold of the PBI-based OSCs, thus favoring photo-induced charge separation and transport at the hybrid heterojunction.[29–31] To this end, the on-surface polymerization of the **PBI-1-COF** was performed using 3D-tungsten oxide nanosheets ($WO_3$ 3D-NS) grown on FTO substrates. $WO_3$ 3D-NS exposing dominant 001 facets are known to facilitate the adsorption of aromatic OSCs with protonated N-doped domains owing to their elevated surface energy and negatively charged surface density.[28]

In detail, the $WO_3$-based electrode was immersed in the reaction mixture (1,2-DCB : *t*-BuOH 50 : 50) under solvothermal conditions at 120 °C for 3 days, according to the optimized synthetic protocol (Fig. 5A), and then washed with organic solvents (tetrahydrofuran and DCM) to remove unreacted monomers and/or small soluble oligomers. SEM experiments on **PBI-1-COF@WO$_3$** reveal the formation of a uniform film on the $WO_3$ 3D-NS surface, exhibiting the same morphology as **PBI-1-COF** (Fig. 5A). The OSC coating on the resulting **PBI-1-COF@WO$_3$** is further confirmed by FT-IR, diffuse reflectance (DR) spectra, and SEM-EDX (Fig. 5A–C, SI Section S5.1, Fig. S14–S16). SEM-EDX elemental mapping highlights the diffused co-localization of the inorganic–organic heterojunction across the vertical section of the electrode (35 μm, Fig. 5B).

Compared to the solution behaviour of **PBI-1** in DCM (Fig. 5C, grey line), the COF arrangement induces a redshift of *ca.* 20 nm in the absorption maximum (**PBI-1** $\lambda_{A_{0-0}} = 552$ nm, **PBI-1-COF-Ph** $\lambda_{A_{0-0}} = 572$ nm) while preserving the vibronic progression characteristic of weakly coupled PBI J-aggregates.[34,71] This spectral evolution is further accompanied by a progressive redshift of the UV-vis absorption onset (**PBI-1** $\lambda_{\text{onset}} = 590$ nm, **PBI-1-COF-Ph** $\lambda_{\text{onset}} = 645$ nm), and results in a remarkable enhancement of the visible-light absorption cross-section, which is an essential feature for sustainable organic semiconductors. These optical signatures support the

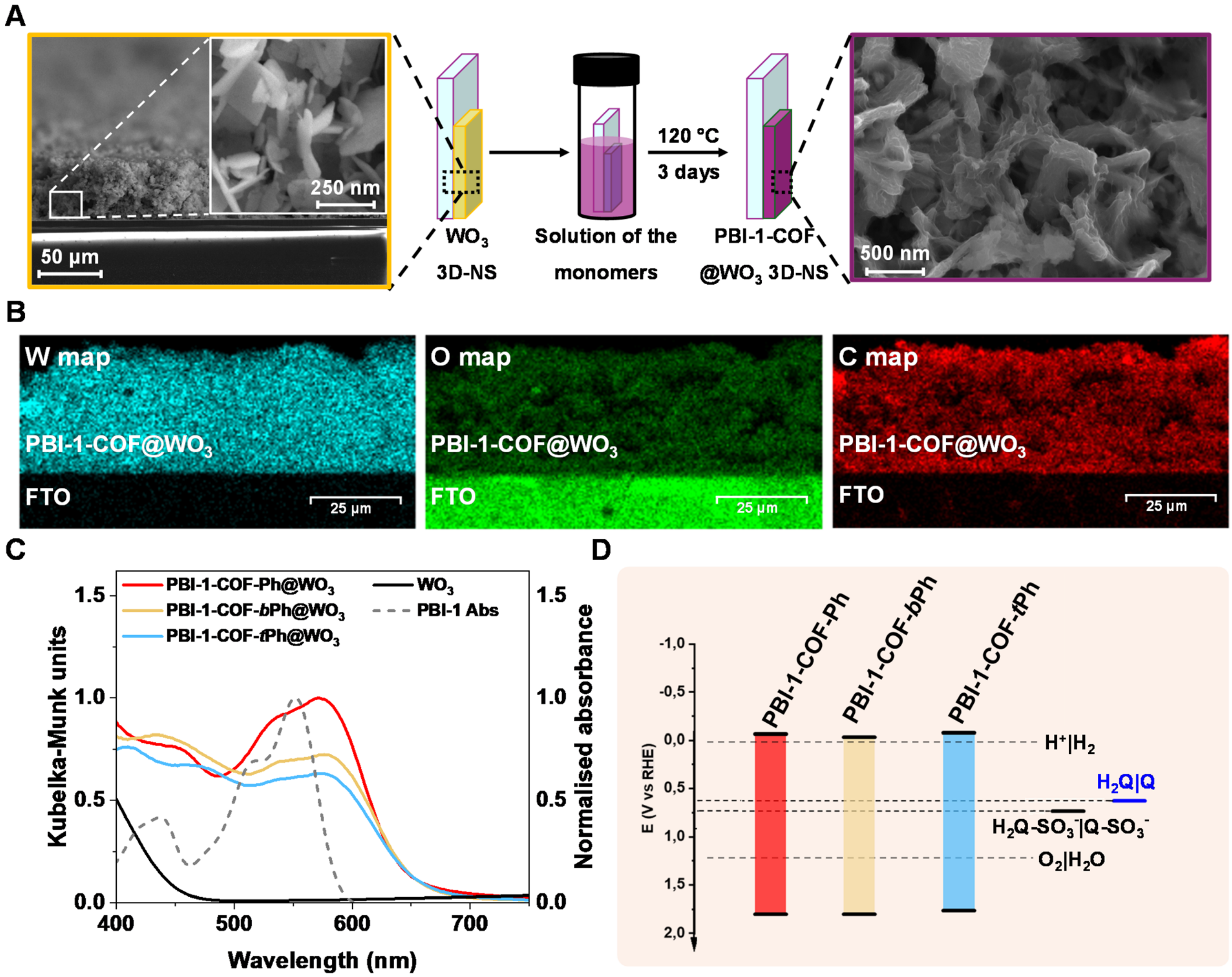

Fig. 5 (A) Schematic representation of the fabrication process of PBI-1-COFs@WO$_3$ photoanodes. Left panel: SEM images of the $WO_3$ 3D-NS electrode. Right panel: SEM image of the PBI-1-COF-Ph@WO$_3$ surface. (B) SEM-EDX mapping of the PBI-1-COF-Ph@WO$_3$ electrode cross-section showing the distributions of W, O and C on the surface. (C) Diffuse reflectance spectra of PBI-1-COF-Ph@WO$_3$ (red trace), PBI-1-COF-*b*Ph@WO$_3$ (yellow trace), PBI-1-COF-*t*Ph@WO$_3$ (blue trace) and $WO_3$ (black trace). Reflectance is converted to Kubelka–Munk units (left axis). The PBI-1 UV-vis solution absorption spectrum (grey trace) is reported for comparison (right axis). (D) Band gaps and band positions of PBI-1-COF-Ph (red box), PBI-1-COF-*b*Ph (yellow box), and PBI-1-COF-*t*Ph (blue box) compared with the oxidation potentials of $H_2Q$ (1,4-hydroquinone) and $H_2Q\text{-}SO_3^-$ (2,5-dihydroxybenzenesulfonate).

formation of a slip-stacked COF architecture, in which the **PBI-1** chromophores adopt an offset π-stacked arrangement along their longitudinal axes with an interplanar slip of >2 Å. This feature is retained upon isoreticular expansion in the COF series, yielding similar absorption envelopes (Fig. 5C).[72–74]

Fluorescence emission is not observed in the **PBI-1-COFs** series, likely explained by the intramolecular quenching of the emissive excited state involving the photo-excited PBI core (acceptor) and the tertiary amine substituents (donor) at the imide position. This multiple donor–acceptor interaction is structurally embedded in the COF topology, is supported by electrochemical data (Fig. 1D) and is further stabilized by the conjugated imine linkage within the COF backbone, which provides an extended π-system for charge delocalization and spatial separation between donor and acceptor sites.[75]

The band edge positions of **PBI-1-COF** materials are identified from a Mott–Schottky plot by conducting capacitance measurements on COF-modified FTO working electrodes (**PBI-1-COF@FTO**, SI, Section S5.2, Fig. S17), confirming the n-type semiconductor behaviour. The Mott–Schottky (M–S) plot provides a flat-band potential ($E_{\mathrm{FB}}$) value of 0.07 ± 0.02 V *vs.* RHE, which is roughly equivalent to a conduction band ($E_{\mathrm{CB}}$) of −0.1 *vs.* RHE, considering a 0.2 V correction factor.[47] Thus, taking into consideration the optical band gap, a valence band ($E_{\mathrm{VB}}$) of 1.9 V *vs.* RHE is estimated, which makes the **PBI-1-COF@WO$_3$** photoanodes suitable for thermodynamic water splitting to hydrogen and oxygen (Fig. 5D).

The photoelectrocatalytic performance of the **PBI-1-COF@WO$_3$** series was probed in acidic water (1 M $H_2SO_4$) using hydroquinones as bio-inspired redox mediators, mimicking the electron/proton relay scheme of natural photosystems. In particular, the photoanodic response of **PBI-1-COF-Ph@WO$_3$** was initially tested against neutral *p*-hydroquinone (**H$_2$Q**, SI, Section S6.1, Fig. S18), featuring a midpoint redox potential within the bandgap of the **PBI-1-COF** materials (Fig. 5D). Photoelectrocatalytic experiments were carried out in a standard three-electrode setup using the **PBI-1-COF@WO$_3$** as the working electrode and irradiating using a solar simulator equipped with an AM1.5G filter and a 490 nm longpass filter to exclude direct excitation of the $WO_3$ layer. Chopped-light linear sweep voltammetry (LSV) experiments were performed in the anodic scan (0.3–0.9 V *vs.* RHE) in the presence of the **H$_2$Q** donor (SI, Section S6.3, Fig. S20). The photoanode displays a photocurrent onset at 0.4 V *vs.* RHE and a dual transient regime with partial recombination at a low applied bias (<0.5 V *vs.* RHE), while reaching optimal charge collection in the range of 0.5–0.9 V *vs.* RHE (SI, Section S6.3, Fig. S20). Photocurrent densities up to 250 ± 10 μA cm$^{-2}$ are obtained at 0.8 V *vs.* RHE and an applied bias, with stable transient behavior up to 250 s under chopped-light chronoamperometry (CLCA, SI, Section S6.4, Fig. S21). Notably, in the absence of the hydroquinone donor or in the presence of its oxidized quinone form (**Q**), the photocurrent density drops significantly, reaching only 50 μA cm$^{-2}$ and 80 μA cm$^{-2}$, respectively (SI, Section S6.4, Fig. S21). The charge separation efficiency was probed in terms of the **H$_2$Q/Q** conversion by long-term photoelectrolysis ($t$ > 14 h) in a divided photoelectrochemical cell to prevent the quinone back-reduction at the counter electrode. Product quantification *via* UV-vis absorption spectroscopy yielded a faradaic efficiency of $\eta = 80\%$ (SI, Section S6.4, Fig. S21). The specific recognition properties of **PBI-1-COF-Ph@WO$_3$** were probed using the anionic hydroquinone sulfonate (**H$_2$Q-SO$_3$$^-$**), which under chopped-light LSV achieves photocurrent values up to 590 ± 20 μA cm$^{-2}$ at 0.8 V *vs.* RHE, corresponding to a 230% enhancement with respect to **H$_2$Q** (Fig. 6A). **PBI-1-COF-Ph@WO$_3$** maintains remarkable stability under diverse illumination regimes during a 22 h operation, with only a 16% photocurrent decrease occurring in the last 12 h period under continuous illumination (see SI Section S6.4, Fig. S22). Indeed, line broadening is observed in the solution $^1$H-NMR spectrum of **H$_2$Q-SO$_3$$^-$** (3 mM in $D_2O$ with 20 mM DCl) upon the addition of **PBI-1-COF-Ph** (0.3 mg mL$^{-1}$), indicating an interaction between the two species (Section S6.4, Fig. S21).[76] This finding is further supported by NMR-DOSY experiments performed in acidic $D_2O$ (DCl 20 mM), where both **H$_2$Q** (3 mM) and **H$_2$Q-SO$_3$$^-$** (3 mM) were analysed in the presence of **PBI-1-COF-Ph** (0.3 mg mL$^{-1}$). The results reveal a clear decrease in the diffusion coefficient exclusively for **H$_2$Q-SO$_3$$^-$**, dropping from $D = 6.2 \times 10^{10}$ m$^2$ s$^{-1}$ to $D = 4.1 \times 10^{10}$ m$^2$ s$^{-1}$ upon COF addition. The consistent decrease in the diffusion coefficient only for the anionic species confirms the notion of a preferential recognition and COF association of the anionic hydroquinone through electrostatic interactions. Along these lines, the impact of the isoreticular COF expansion on the photocurrent response was investigated by performing CLCA experiments on **PBI-1-COF-*b*Ph@WO$_3$** and **PBI-1-COF-*t*Ph@WO$_3$** photoanodes at 0.8 V *vs.* RHE in the presence of **H$_2$Q-SO$_3$$^-$** (Fig. 6B). A progressive photocurrent decline is observed across the series, with **PBI-1-COF-*b*Ph** and **PBI-1-COF-*t*Ph** yielding photocurrent densities, respectively, of 240 ± 40 μA cm$^{-2}$ and 180 ± 30 μA cm$^{-2}$ (S1, Section S6.5–6, Fig. S22 and S23). The evaluation of the photocurrent response was performed upon the normalization of the COF loading on the $WO_3$-based electrodes, considering the resulting optical density from DR spectra, whereby **PBI-1-COF-Ph** was used as a reference (100%), followed by **PBI-1-COF-*b*Ph** (73% ± 5%) and **PBI-1-COF-*t*Ph** (62% ± 4%). The loading variation is likely ascribed to differences in solubility and polymerization kinetics associated with the increasing length of the diamine linkers, possibly affecting the growth of the COF film on the $WO_3$-based electrodes.[49,50,77] It turns out that the normalized photocurrent density $J_{\mathrm{eff}}$ marks a distinct advantage for the **PBI-1-COF-Ph** term, overarching the isostructural homologues that level off at approximately halved values (Fig. 6C). This evidence points out that the photoelectrochemical processes are governed by kinetic factors *vis-à-vis* the similar thermodynamic requirements of the COF series (Fig. 5D).

One such factor may be related to the increasing hydrophobic character of the frameworks with extended aromatic linkers. The poly-aromatic linkers can potentially hinder the diffusion of hydrophilic and anionic redox mediators like **H$_2$Q-SO$_3$$^-$** into the COF pores. To verify this hypothesis, we conducted a cross-comparison of thermogravimetric analysis (TGA) throughout the COF series before and after prolonged water exposure. The results reveal that **PBI-1-COF-Ph** exhibits

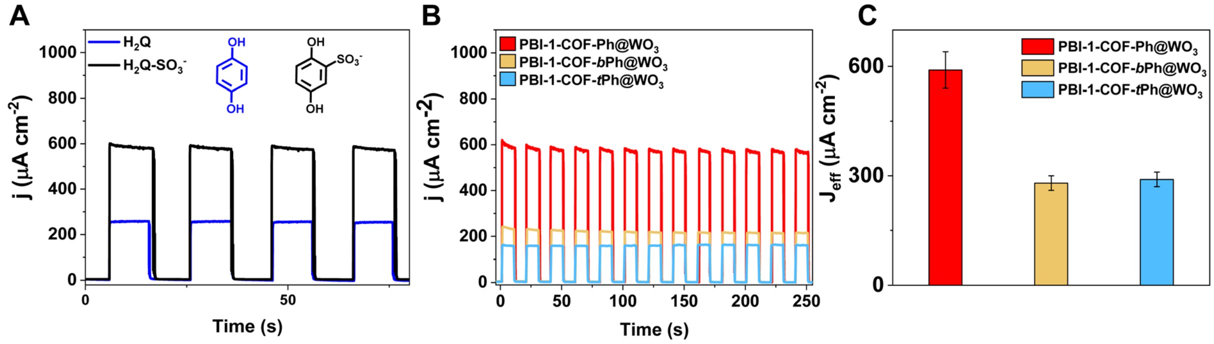

Fig. 6 (A) Representative chopped light chronoamperometries (CLCAs) of **PBI-1-COF-Ph@$WO_3$** with 0.1 M **$H_2Q$** (blue trace) or 0.1 M **$H_2Q$-$SO_3^-$** (black trace). (B) Representative CLCAs for **PBI-1-COF-Ph@$WO_3$** (red trace), **PBI-1-COF-*b*Ph@$WO_3$** (yellow trace), and **PBI-1-COF-*t*Ph@$WO_3$** (blue trace) in the presence of 0.1 M **$H_2Q$-$SO_3^-$**. Experimental conditions for CLCA: 0.8 V *vs.* RHE, 1 M $H_2SO_4$, scan rate = 10 mV s$^{-1}$, 10 s light and 10 s dark; the illumination was provided by a solar simulator equipped with an AM 1.5G filter, 100 mW cm$^{-2}$, and a 490 nm longpass filter. Values reported are the average photocurrent densities (registered in triplicates) of the three **PBI-1-COF@$WO_3$** systems. (C) Comparison of **PBI-1-COF@$WO_3$** photocurrent performances normalized on the **PBI-1-COF** loading estimated by the relative absorbance of the photoanodes (**PBI-1-COF-Ph**, red trace; **PBI-1-COF-*b*Ph**, yellow trace; and **PBI-1-COF-*t*Ph**, blue trace).

a greater fraction of surface-bound water, accounting for approximately 4% of the total weight, than **PBI-1-COF-*b*Ph** and **PBI-1-COF-*t*Ph** (0.9% and 0.7%, respectively), as indicated by the weight loss observed between 40 °C and 100 °C.[78,79] (SI, Section S6.7, Fig. S24 and S25).

To further investigate the discrepancy observed in the photoelectrochemical performance, the **PBI-1-COFs** were incubated in an acidified acetonitrile/$H_2O$ 100 : 1 mixture containing **$H_2Q$-$SO_3^-$** and then recovered by filtration. The FT-IR spectra of the recovered solids show distinct modifications in **PBI-1-COF-Ph**, suggesting the effective absorption of the hydroquinone, as the characteristic bands of **$H_2Q$-$SO_3^-$** can be noted ($\nu$ = 1081 and 1021 cm$^{-1}$, assigned to the asymmetric and symmetric stretching of O═S═O, respectively, and $\nu$ = 861 and 822 cm$^{-1}$, assigned to the out-of-plane bending of C–H groups in 1,2,4-tri-substituted benzenes; SI, Section S6.8, Fig. S28).[80,81] On the contrary, **PBI-1-COF-*b*Ph** and **PBI-1-COF-*t*Ph** exhibit no significant changes, pointing to less efficient host-guest interactions (SI, Section S6.8, Fig. S26). These findings underscore the importance of precision chemistry strategies to tailor the COF properties in terms of molecular recognition that can direct the overall photoelectrocatalytic performance of the system.

## 3. Conclusions

The first series of covalent organic frameworks encoding full bay-substituted perylene bisimide chromophores has been designed with a unique core-twisted π-conjugation, a broad visible-light cross-section (400–700 nm), n-type semiconductor behaviour with high bandgaps (1.9 eV), molecular control over the N-doped site distribution, surface recognition of anionic co-factors triggered by protonation equilibria, and isoreticular expansion upon the modulation of poly-aromatic diamine linkers ($n$ = 1–3). Chiral dislocation signatures have been clearly identified for **PBI-1-COF-Ph** ($n$ = 1), which evolves to quasi mono-dispersed spherical micro-particles ($D$ = 700 ± 100 nm) with an onion-like crystalline architecture, formed upon the progressive folding of staggered π-nano-stacks. The resulting optical envelope marks a definite red-shift to low energy wavelengths, in agreement with the prevalent J-type coupling of the PBI chromophores (inter-planar slip of >2 Å along the PBI longitudinal axes). The manipulation of the multi-chromophore exciton coupling, spatial distribution and framework delocalization is crucial to the regulation of the organic semiconductor optoelectronics. The **PBI-1-COF** structure prevents major losses through excimer formation and fluorescence decay. On the contrary, their engineering on high surface area $WO_3$ 3D-NS photoanodes promotes photo-induced charge separation and transport, with record photocurrent densities up to 590 ± 50 μA cm$^{-2}$ using low energy photons ($\lambda$ > 490 nm),[82] 1 sun irradiation, an applied bias of 0.8 V *vs.* RHE and remarkable stability for long-term photoelectrolysis (>20 h; SI, Section S6.4, Fig. S21, S22 and Section S12, Tables S6 and S7). The use of anionic hydroquinones as bio-inspired redox co-factors reveals the key recognition properties of the **PBI-1-COF** as molecular OSCs, directed by complementary charge interactions as well as by the COF amphiphilic domains.

Our study highlights that a synergistic interplay of structural effectors, harnessing supramolecular and precision chemistry methods, sets a unique driver for the development of next-generation COF-based OSCs for application in photocatalytic water splitting,[5,83] water remediation and redox flow batteries.[6,7,84]

The key role of PBI-induced chiral dislocations in **COF** materials will be further explored to address chiral-induced spin selectivity (CISS) and its impact on charge transport and photocurrent generation.[85–88]

## Author contributions

M. B. conceived this work and was responsible for funding acquisition. J. L. designed and prepared the $WO_3$ 3D-NS substrates. S. M., G. B. and S. Bo. performed and discussed the BET analysis. S. Br. and A. C. performed and discussed the solid-state NMR experiments. L. C. synthesized **PBI-1**, and the relative materials. L. C., T. G. and D. R.-G. performed the experiments, analysed the data and drafted the manuscript. F. R. participated in the discussion of experimental results. T. G., D. R.-G. and M. B. supervised the project and finalized the manuscript. All authors reviewed and commented on the manuscript.

## Conflicts of interest

There are no conflicts to declare.

## Data availability

The data supporting this article have been included as part of the SI.

Supplementary information is available and includes synthetic procedures, characterization data, computational results, and full photoelectrochemical experiments for the materials presented in this manuscript. See DOI: **https://doi.org/10.1039/d5ta05253j**.

## Acknowledgements

Andrea Basagni is acknowledged for TEM and SEM imaging. PXRD experiments were performed using a Bruker AXS D8 ADVANCE Plus diffractometer, funded by the MIUR- "Dipartimenti di Eccellenza" Grant "NExuS". This research was funded by the National Recovery and Resilience Plan (NRRP), Mission 4 Component 2 Investment1.3 -Call for tender No. 1561 of 11. 10. 2022 of Ministero dell'Università e della Ricerca (MUR); by the European Union – NextGenerationEU, Project code PE000002, Project title "Network 4 Energy Sustainable Transition-NEST CUP C93C22005230007"; by the European Innovation Council project PLANKT-ON (Plankton-Like Protocells for Artificial Photosynthesis Targeting Carbon-Neutral Energy Vectors, Pathfinder-Open 2022, grant agreement no. 101099192); and by the Ministero dell'Università e della Ricerca PRIN 2022 NANOARC, 20228YFRNL and HYSTAR (no. H53D23004720006) projects. Open Access publishing was facilitated by Università degli Studi di Padova, as part of the RSC-CRUI-CARE agreement.

## Notes and references

1 L. Bai, N. Wang and Y. Li, *Adv. Mater.*, 2022, **34**, 2102811.
2 B. Sung, A. de la Cotte and E. Grelet, *Nat. Commun.*, 2018, **9**, 1405.
3 J. Kosco, F. Moruzzi, B. Willner and I. McCulloch, *Adv. Energy Mater.*, 2020, **10**, 2001935.
4 J. Chen, W. Zhang, L. Wang and G. Yu, *Adv. Mater.*, 2023, **35**, 2210772.
5 H. Hou, K. Wu, X. Chen, X. Liu and Y. Zhao, *J. Am. Chem. Soc.*, 2025, **147**(31), 27835–27846.
6 B. Yang, L. Hoober-Burkhardt, F. Wang, G. K. S. Prakash and S. R. Narayanan, *J. Electrochem. Soc.*, 2014, **161**, A1371.
7 F. Wang, H. Sheng, W. Li, J. B. Gerken, S. Jin and S. S. Stahl, *ACS Energy Lett.*, 2021, **6**, 1533–1539.
8 Q. Wang and K. Domen, *Chem. Rev.*, 2020, **120**, 919–985.
9 A. Hofmann, M. Schmid and W. Brütting, *Adv. Opt. Mater.*, 2021, **9**, 2101004.
10 L. Cognigni, T. Gobbato, E. Benazzi, L. Paoloni, B. D. Vizio, R. Bonetto, F. Rigodanza, A. Bonetto, S. Agnoli, M. Bonchio and P. Costa, *ChemSusChem*, 2025, **18**, e202401977.
11 T. Gobbato, M. Sicignano, B. Di Vizio, F. De Biasi, D. Rosa-Gastaldo, A. Bonetto and P. Costa, *ChemCatChem*, 2024, **16**, e202301732.
12 M. Sicignano, T. Gobbato, R. Bonetto, P. Centomo, B. Di Vizio, F. De Biasi, D. Rosa-Gastaldo, C. Pierantoni, A. Bonetto, A. Glisenti and P. Costa, *Adv. Sustainable Syst.*, 2025, **9**, 2400653.
13 T. Banerjee and B. V. Lotsch, *Nat. Chem.*, 2018, **10**, 1175–1177.
14 T. Banerjee, F. Podjaski, J. Kröger, B. P. Biswal and B. V. Lotsch, *Nat. Rev. Mater.*, 2020, **6**, 168–190.
15 T. Banerjee, K. Gottschling, G. Savasci, C. Ochsenfeld and B. V. Lotsch, *ACS Energy Lett.*, 2018, **3**, 400–409.
16 F. Schlosser, J. Sung, P. Kim, D. Kim and F. Würthner, *Chem. Sci.*, 2012, **3**, 2778–2785.
17 F. Würthner, *Chem. Commun.*, 2004, 1564–1579.
18 F. Würthner, C. R. Saha-Möller, B. Fimmel, S. Ogi, P. Leowanawat and D. Schmidt, *Chem. Rev.*, 2016, **116**, 962–1052.
19 A. Nowak-Król and F. Würthner, *Org. Chem. Front.*, 2019, **6**, 1272–1318.
20 F. Würthner, *Pure Appl. Chem.*, 2006, **78**, 2341–2349.
21 S. E. Penty, G. R. F. Orton, D. J. Black, R. Pal, M. A. Zwijnenburg and T. A. Barendt, *J. Am. Chem. Soc.*, 2024, **146**, 5470–5479.
22 P. Osswald, M. Reichert, G. Bringmann and F. Würthner, *J. Org. Chem.*, 2007, **72**, 3403–3411.
23 P. Osswald and F. Würthner, *J. Am. Chem. Soc.*, 2007, **129**, 14319–14326.
24 F. Auras, L. Ascherl, V. Bon, S. M. Vornholt, S. Krause, M. Döblinger, D. Bessinger, S. Reuter, K. W. Chapman, S. Kaskel, R. H. Friend and T. Bein, *Nat. Chem.*, 2024, **16**, 1373–1380.
25 Z. Li, J. Jiao, W. Fu, K. Gao, X. Peng, Z. Wang, H. Zhuo, C. Yang, M. Yang, G. Chang, L. Yang, X. Zheng, Y. Yan, F. Chen, M. Zhang, Z. Meng and X. Shang, *Angew. Chem., Int. Ed.*, 2024, **63**, e202412977.
26 Y. Jin, X. Liu, C. Qu, C. Li, H. Wang, X. Zhan, X. Cao, X. Li, B. Yu, Q. Zhang, D. Qi and J. Jiang, *Chin. J. Catal.*, 2024, **57**, 171–183.
27 W. Gao, Y. Bai, X. Wang, H. Fu, P. Zhao, P. Zhu and J. Yu, *J. Colloid Interface Sci.*, 2024, **663**, 262–269.
28 J. Liu, I. Crea, T. Gobbato, F. Rigodanza, G. A. Rizzi, E. Benazzi and M. Bonchio, *Adv. Energy Sustainability Res.*, 2025, 2500184.
29 J. T. Kirner and R. G. Finke, *ACS Appl. Mater. Interfaces*, 2017, **9**, 27625–27637.
30 M. Bonchio, Z. Syrgiannis, M. Burian, N. Marino, E. Pizzolato, K. Dirian, F. Rigodanza, G. A. Volpato, G. La

Ganga, N. Demitri, S. Berardi, H. Amenitsch, D. M. Guldi, S. Caramori, C. A. Bignozzi, A. Sartorel and M. Prato, *Nat. Chem.*, 2019, **11**, 146–153.

31 F. Ronconi, Z. Syrgiannis, A. Bonasera, M. Prato, R. Argazzi, S. Caramori, V. Cristino and C. A. Bignozzi, *J. Am. Chem. Soc.*, 2015, **137**, 4630–4633.

32 R. K. Dubey, N. Westerveld, F. C. Grozema, E. J. R. Sudhölter and W. F. Jager, *Org. Lett.*, 2015, **17**, 1882–1885.

33 P. Spenst, R. M. Young, B. T. Phelan, M. Keller, J. Dostál, T. Brixner, M. R. Wasielewski and F. Würthner, *J. Am. Chem. Soc.*, 2017, **139**, 2014–2021.

34 D. Bialas, E. Kirchner, M. I. S. Röhr and F. Würthner, *J. Am. Chem. Soc.*, 2021, **143**, 4500–4518.

35 C. Arantes, M. Scholz, R. Schmidt, V. Dehm, M. L. M. Rocco, A. Schöll, F. Reinert and F. Würthner, *Appl. Phys. A*, 2012, **108**, 629–637.

36 H. Wu, H. Wang, L. Xue, Y. Shi and X. Li, *J. Phys. Chem. B*, 2010, **114**, 14420–14425.

37 T. Ide, J. P. Barham, M. Fujita, Y. Kawato, H. Egami and Y. Hamashima, *Chem. Sci.*, 2018, **9**, 8453–8460.

38 R. Renner, B. Mahlmeister, O. Anhalt, M. Stolte and F. Würthner, *Chem.–Eur. J.*, 2021, **27**, 11997–12006.

39 L. Kiss and S. Kunsági-Máté, *C. R. Chim.*, 2019, **22**, 557–561.

40 P. Costa, A. Vega-Peñaloza, L. Cognigni and M. Bonchio, *ACS Sustainable Chem. Eng.*, 2021, **9**, 15694–15721.

41 N. A. Khan, R. Zhang, X. Wang, L. Cao, C. S. Azad, C. Fan, J. Yuan, M. Long, H. Wu, M. A. Olson and Z. Jiang, *Nat. Commun.*, 2022, **13**, 3169.

42 P. J. Waller, Y. S. AlFaraj, C. S. Diercks, N. N. Jarenwattananon and O. M. Yaghi, *J. Am. Chem. Soc.*, 2018, **140**, 9099–9103.

43 X. Wu, B. Wang, Z. Yang and L. Chen, *J. Mater. Chem. A*, 2019, **7**, 5650–5655.

44 M. Matsumoto, R. R. Dasari, W. Ji, C. H. Feriante, T. C. Parker, S. R. Marder and W. R. Dichtel, *J. Am. Chem. Soc.*, 2017, **139**, 4999–5002.

45 Y. Liu, C. Yang, Y. Li, Y. Li, S. Wang, J. Zhuang, H. Liu, N. Wang, X. He, Y. Li and D. Zhu, *Macromolecules*, 2005, **38**, 716–721.

46 H. Lyu, H. Li, N. Hanikel, K. Wang and O. M. Yaghi, *J. Am. Chem. Soc.*, 2022, **144**, 12989–12995.

47 A. J. Howarth, A. W. Peters, N. A. Vermeulen, T. C. Wang, J. T. Hupp and O. K. Farha, *Chem. Mater.*, 2017, **29**, 26–39.

48 S. Van Gele, S. Bette and B. V. Lotsch, *JACS Au*, 2025, **5**, 388–398.

49 K. Xiong, Y. Wang, F. Zhang, X. Li and X. Lang, *Appl. Catal., B*, 2023, **322**, 122135.

50 X. Li, T. Zhao, F. Wang, W. Wu, Y. Sun, H. Ren and F. Sun, *Chem. Sci.*, 2025, **16**, 7339–7346.

51 C. Gao, X. Guan, M. Zhang, H. Hu, L. Chen, C. Sun, C. Zhang, Y. Du and B. Hu, *Macromol. Rapid Commun.*, 2023, **44**, 2300311.

52 J. Ming, A. Liu, J. Zhao, P. Zhang, H. Huang, H. Lin, Z. Xu, X. Zhang, X. Wang, J. Hofkens, M. B. J. Roeffaers and J. Long, *Angew. Chem., Int. Ed.*, 2019, **58**, 18290–18294.

53 F. Wen, X. Wu, X. Li and N. Huang, *Chem.–Eur. J.*, 2023, **29**, e202302399.

54 T. Banerjee, F. Haase, S. Trenker, B. P. Biswal, G. Savasci, V. Duppel, I. Moudrakovski, C. Ochsenfeld and B. V. Lotsch, *Nat. Commun.*, 2019, **10**, 2689.

55 K. Dey, M. Pal, K. C. Rout, S. Kunjattu H, A. Das, R. Mukherjee, U. K. Kharul and R. Banerjee, *J. Am. Chem. Soc.*, 2017, **139**, 13083–13091.

56 Y. Zhao, C. Zhang, D. D. Kohler, J. M. Scheeler, J. C. Wright, P. M. Voyles and S. Jin, *Science*, 2020, **370**, 442–445.

57 Q. Zheng, C. Yang, D. Lee, K. C. Bustillo and H. Zheng, *Microsc. Microanal.*, 2023, **29**, 1746–1747.

58 Z. Lei, Q. Yang, Y. Xu, S. Guo, W. Sun, H. Liu, L.-P. Lv, Y. Zhang and Y. Wang, *Nat. Commun.*, 2018, **9**, 576.

59 Y. Li, M. Zhang, X. Guo, R. Wen, X. Li, X. Li, S. Li and L. Ma, *Nanoscale Horiz.*, 2018, **3**, 205–212.

60 J. Guo, Y. Xu, S. Jin, L. Chen, T. Kaji, Y. Honsho, M. A. Addicoat, J. Kim, A. Saeki, H. Ihee, S. Seki, S. Irle, M. Hiramoto, J. Gao and D. Jiang, *Nat. Commun.*, 2013, **4**, 2736.

61 C. Liu, Z. Wang, L. Zhang and Z. Dong, *J. Am. Chem. Soc.*, 2022, **144**, 18784–18789.

62 B. Dhokale, K. Coe-Sessions, M. J. Wenzel, A. E. Davies, T. Kelsey, J. A. Brant, L. de S. Oliveira, B. A. Parkinson and J. O. Hoberg, *J. Am. Chem. Soc.*, 2024, **146**, 33048–33055.

63 Q. Zheng, X. Li, Q. Zhang, D. Lee, H. Mao, C. Yang, K. C. Bustillo, J. A. Reimer, Y. Liu, J. Jiang and H. Zheng, *Mater. Today*, 2022, **60**, 98–105.

64 S. Xiong, Y. Zhang, W. Zhang, N. Yang, F. Lv, J. Guo, X. Cui, K. Fang, M. Chen, C. Wang, C. Hua, R. Zhang, J. Chu and J. Xu, *J. Electron. Mater.*, 2024, **53**, 2656–2665.

65 L. Yao, A. Rodríguez-Camargo, M. Xia, D. Mücke, R. Guntermann, Y. Liu, L. Grunenberg, A. Jiménez-Solano, S. T. Emmerling, V. Duppel, K. Sivula, T. Bein, H. Qi, U. Kaiser, M. Grätzel and B. V. Lotsch, *J. Am. Chem. Soc.*, 2022, **144**, 10291–10300.

66 J.-H. Chen, X. Wang, H. Chen, D. Jiang, J. Liu and H. Zhou, *Adv. Funct. Mater.*, 2025, **35**(31), 2424871.

67 S. Mondal, B. Mohanty, M. Nurhuda, S. Dalapati, R. Jana, M. Addicoat, A. Datta, B. K. Jena and A. Bhaumik, *ACS Catal.*, 2020, **10**, 5623–5630.

68 D. Zhao, Q. Wu, Z. Cai, T. Zheng, W. Chen, J. Lu and L. Yu, *Chem. Mater.*, 2016, **28**, 1139–1146.

69 D. Sun, D. Meng, Y. Cai, B. Fan, Y. Li, W. Jiang, L. Huo, Y. Sun and Z. Wang, *J. Am. Chem. Soc.*, 2015, **137**, 11156–11162.

70 J. Wu, D. He, L. Zhang, Y. Liu, X. Mo, J. Lin and H. Zhang, *Org. Lett.*, 2017, **19**, 5438–5441.

71 H. Langhals and W. Jona, *Angew. Chem., Int. Ed.*, 1998, **37**, 952–955.

72 M. Hecht and F. Würthner, *Acc. Chem. Res.*, 2021, **54**, 642–653.

73 A. Oleson, T. Zhu, I. S. Dunn, D. Bialas, Y. Bai, W. Zhang, M. Dai, D. R. Reichman, R. Tempelaar, L. Huang and F. C. Spano, *J. Phys. Chem. C*, 2019, **123**, 20567–20578.

74 N. J. Hestand and F. C. Spano, *Chem. Rev.*, 2018, **118**, 7069–7163.

75 Y. Wang, Y.-Z. Cheng, K.-M. Wu, D.-H. Yang, X.-F. Liu, X. Ding and B.-H. Han, *Angew. Chem., Int. Ed.*, 2023, **62**, e202310794.

76 A. Cesari, D. Rosa-Gastaldo, A. Pedrini, F. Rastrelli, E. Dalcanale, R. Pinalli and F. Mancin, *Chem. Commun.*, 2022, **58**, 10861–10864.

77 Z. Ou, B. Liang, Z. Liang, F. Tan, X. Dong, L. Gong, P. Zhao, H. Wang, Y. Zou, Y. Xia, X. Chen, W. Liu, H. Qi, U. Kaiser and Z. Zheng, *J. Am. Chem. Soc.*, 2022, **144**, 3233–3241.

78 A. A. Apostolov, S. Fakirov, E. Vassileva, R. D. Patil and J. E. Mark, *J. Appl. Polym. Sci.*, 1999, **71**, 465–470.

79 X. Mu, J. Zhan, X. Feng, B. Yuan, S. Qiu, L. Song and Y. Hu, *ACS Appl. Mater. Interfaces*, 2017, **9**, 23017–23026.

80 A. Singh, S. Bisoi, S. Banerjee, H. Komber and B. Voit, *Macromol. Mater. Eng.*, 2017, **302**, 1700208.

81 D. G. O'Sullivan, *Spectrochim. Acta*, 1960, **16**, 762–764.

82 T. Gobbato, G. A. Volpato, A. Sartorel and M. Bonchio, *Chem. Sci.*, 2023, **14**, 12402–12429.

83 Note: preliminary results show hydrogen evolution ([$H_2$ rate] $= 0.15$ μmol $h^{-1}$) by the platinum-free **PBI-1-COF-Ph** photocatalyst in 1 M $H_2SO_4$ under white led illumination ($I_{ph} = 500$ mW $cm^{-2}$, 5 Suns) in the presence of ascorbic acid (0.6 M), Fig. S31.

84 M. B. Asif, S. Kim, T. S. Nguyen, J. Mahmood and C. T. Yavuz, *J. Am. Chem. Soc.*, 2024, **146**, 3567–3584.

85 B. P. Bloom, Y. Paltiel, R. Naaman and D. H. Waldeck, *Chem. Rev.*, 2024, **124**, 1950–1991.

86 W. Mtangi, V. Kiran, C. Fontanesi and R. Naaman, *J. Phys. Chem. Lett.*, 2015, **6**, 4916–4922.

87 S.-J. Zheng, H. Chen, S.-Q. Zang and J. Cai, *Matter*, 2025, **8**, 101924.

88 K. Chae, N. A. R. Che Mohamad, J. Kim, D.-I. Won, Z. Lin, J. Kim and D. Ha Kim, *Chem. Soc. Rev.*, 2024, **53**, 9029–9058.